CRYSTAL GROWTH & DESIGN

pubs.acs.org/crystal

Article

Disorderly Conduct of Benzamide IV: Crystallographic and Computational Analysis of High Entropy Polymorphs of Small Molecules

Noalle Fellah, Alexander G. Shtukenberg,* Eric J. Chan, Leslie Vogt-Maranto, Wenqian Xu, Chao Li, Mark E. Tuckerman,* Bart Kahr,* and Michael D. Ward*

Cite This: *Cryst. Growth Des.* 2020, 20, 2670−2682

Read Online

ACCESS | Metrics & More | Article Recommendations | Supporting Information

ABSTRACT: Benzamide, a simple derivative of benzoic acid and a common intermediate of pharmaceutical compounds, was reported to form two polymorphs in 1832, but the single crystal structure of the more stable form was not solved until 1959. Nearly 50 years later, the second form was characterized by powder diffraction, followed shortly thereafter by characterization of a third form, a polytype of the most thermodynamically stable Form **I**. These two new forms, Forms **II** and **III**, are metastable. Herein, we describe a fourth polymorph, Form **IV**, discovered by melt crystallization concurrently with its crystallization under confinement at small length scales (<10 nm), where it is stable indefinitely. Form **III** exists under confinement in larger pores, and melting point data for different pore sizes corroborate the existence of Form **IV** below 10 nm. Form **IV** is highly disordered, precluding indexing of powder diffraction data other than *hk*0 reflections. Nonetheless, a combination of powder X-ray diffraction and computational crystal structure prediction reveals that Form **IV** contains a 2D motif resembling that of Form **II**, but with long-range order in the third dimension masked by ubiquitous stacking faults. This approach relies on distilling a large number of candidate structures to a few possible disorder models based on benzamide tetrads that organize in 2D parquet-like tiles, with organization along the third dimension, that can be modeled with various stacking fault configurations having distinct intermolecular interactions and translations in the dimension orthogonal to the tiling planes. These observations reveal a bewildering crystallographic complexity for such a simple molecule. Nonetheless, the approach described herein demonstrates that challenging structures that may be abandoned prematurely because of poor crystallinity, twinning, or disorder can be solved.

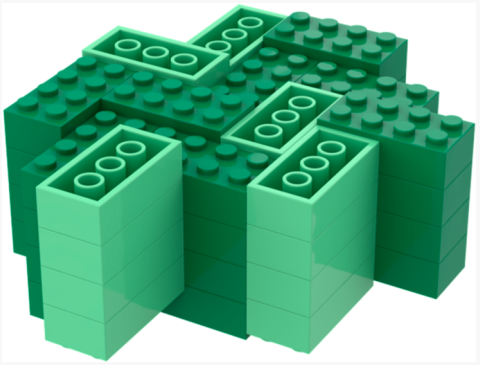

INTRODUCTION

Wöhler and von Liebig, while struggling to make sense of constitution in organic compounds, cooled a boiling, aqueous solution of benzamide and recorded the remarkable transformation of silky needles into well-formed rhombic crystals.[1] Thus, benzamide (Scheme 1), now recognized as a common intermediate for pharmaceutical compounds,[2−5] became the first reported example of polymorphism of molecular crystals.[6] The single crystal structure of the stable (rhombic) Form **I** was not solved until 1959 and was assigned as monoclinic.[7] Nearly 50 years later, the transient Form **II** was prepared *in situ* as a mixture with **I**, and a structure was extracted from powder X-ray diffraction (PXRD) data.[8,9] A third metastable polymorph (Form **III**), revealing a polytypic relationship to Form **I**, was characterized shortly afterward.[10,11] Yet, another polymorph has been suggested by crystal structure prediction (CSP) but not found experimentally.[12] The characterization of the metastable benzamide polymorphs is complicated further by the formation of bi- or triphasic mixtures, requiring extensive optimization of crystallization protocols to minimize secondary nucleation of Form **I**.[11,13,14] Computational studies suggested an alternative structure for Form **II**, attributing the previous structure solution to insufficient data owing to the preferred orientations of needle-like crystals and the associated weak intensity of *hkl* reflections with $l \neq 0$.[15] Absent or weak

Scheme 1. Benzamide Structure

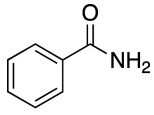

Benzamide

Received: January 22, 2020
Revised: February 26, 2020
Published: March 11, 2020

reflections, however, also can be explained by stacking disorder. While stacking faults are well-documented for minerals or synthetic zeolites,[16−20] they are less frequently reported for molecular solids.[21,22] The disorder unavoidably leads to poor quality or incomplete data, thereby frustrating structure solution using conventional characterization methods. Recently crystal structure prediction and density functional theory have emerged as powerful tools for overcoming limitations in small molecule structure determination[23−26] and for providing further insight into molecular packing interactions.[27,28] These reports, however, have not addressed stacking disorder in molecular solids.

We report herein a new metastable polymorph of benzamide. The new form, denoted here as Form **IV**, was discovered by melt crystallization using optical microscopy concurrent with its crystallization under nanoconfinement. It was confirmed as a unique polymorph by powder X-ray diffraction (PXRD), Raman spectroscopy, and differential scanning calorimetry. Melt crystallization or confinement produced Form **IV** with negligible amounts of contamination by other phases, enabling acquisition of powder data corresponding to a single phase. The PXRD data indicated a high degree of order in one dimension, but the absence of reflections other than *hk*0 suggested disorder in the perpendicular plane. Nonetheless, a combination of PXRD and crystal structure simulation reveals that Form **IV** contains a 2D motif resembling that of Form **II**, but with long-range order in the third dimension masked by ubiquitous stacking faults. This approach relies on distilling a large number of candidate structures to a few possible disorder models based on benzamide tetrads that organize in 2D parquet-like tiles, with organization along the third dimension, that can be modeled with various stacking fault configurations characterized by different intermolecular interactions and translations orthogonal to the parquet tiling planes. This combined experimental−computational approach demonstrates that challenging structures that may be abandoned prematurely because of poor crystallinity, twinning, or disorder can be solved.

EXPERIMENTAL SECTION

Materials and Methods. Benzamide (C_7H_7NO, 99%) was purchased from Sigma-Aldrich (St. Louis, Missouri) and was used without further purification. Controlled pore glass (CPG), a borate−silicate composite glass, from which the borate phase is leached to produce a silica glass bead with a random pore network, was obtained from Biosearch Technologies (Petaluma, CA) with nominal pore sizes of 35, 50, 100, and 200 nm. Porous glass with nominal pore sizes of 4 and 8 nm were purchased from Sigma-Aldrich. The CPG manufacturer specifications are provided in Table S1. All porous glasses were washed with nitric acid prior to use, then washed with deionized water and dried for 12 h under a vacuum. The acid-washed matrices were stored under air in a desiccator.

Crystal Growth. Form **IV** was prepared by melting 2−4 mg of benzamide powder (mp = 125−128 °C) in the presence of natural resins between two glass coverslips on a Kofler bench and rapidly cooling to room temperature (ca. 20 °C). It has been suggested that the addition of resins, such as Canada balsam or gum mastic, can suppress crystal growth until high crystallization driving forces can be achieved at large undercoolings.[29] The amount of resin can vary, from 10 to 30 wt %, and in all cases spherulites corresponding to Form **IV** were observed. The porous glass beads were mixed with benzamide bulk crystals, heated above the benzamide T_m of 130 °C, and allowed to absorb the benzamide by capillary action for 2 min while heating in the DSC instrument. Cooling these nanoporous matrices below the melting point of benzamide results in benzamide nanocrystals embedded within the nanopores, as evident from Bragg peak assignments to benzamide in PXRD data collected on the matrices. Although the extent of pore filling has been reported to have minimal effect on the change of melting temperature,[30,31] overfilling was avoided to prevent thermal signatures of bulk material. The mass ratio of benzamide and CPG and the manufacturer provided pore volume were used to calculate that 67−70% of the pores were filled. The heating and cooling of the benzamide−matrix mixtures were performed with a differential scanning calorimeter at 10 °C/min. Differential scanning calorimetry (DSC) was performed on a Pyris-1 (PerkinElmer Inc., Wellsley, Massachusetts) differential scanning calorimeter. An indium standard was used to calibrate the instrument, and nitrogen was used as the purge gas. Enthalpies were calculated by integrating the areas under the peaks after defining a baseline. Metastable **II** was prepared by evaporation of ethanol solution (140 mg/mL). The benzamide obtained commercially was confirmed by PXRD as Form **I**. Form **III** was obtained as the transformation product of Form **IV** formed from the melt.

X-ray Diffraction. Two-dimensional X-ray microdiffraction (2D μ-XRD) was performed with a Bruker D8 Discover General Area Detector Diffraction System (GADDS) equipped with a VÅNTEC-2000 2D detector and Cu $K\alpha$ source (λ = 1.54178 Å). The X-ray beam was monochromated with a graphite crystal and collimated with a 0.5 mm capillary collimator (MONOCAP). Form **IV** was measured on a glass slide with the coverslip removed. CPG beads consisting of benzamide nanocrystals were loaded into a Kapton 0.8 capillary for measurement. High signal-to-noise ratio synchrotron powder diffraction data was collected for Form **IV** on the 17-BM beamline of the Advanced Photon Source, Argonne National Laboratory, at a wavelength of 0.45212 Å using a PerkinElmer PE1621 area detector. The sample−detector distance was 800 mm, and the measurement covered the angular range 2θ = 0.8−18.8°. A Kapton 1.0 mm capillary was loaded with benzamide powder, which was then melted by heating at ca. 150 °C (above T_m = 130 °C) then rapidly cooled down to 100 K using an Oxford 700+ Cooler and measured at the same temperature. High-resolution synchrotron powder diffraction data of Form **IV** were collected at beamline 11-BM of the Advanced Photon Source, Argonne National Laboratory, using a wavelength of 0.412827 Å. Discrete detectors covering an angular range from −6 to 16° 2θ were scanned over a 34° 2θ range, with data points collected every 0.001° 2θ and scan speed of 0.01°/s. A few milligrams of benzamide mixture with ca. 20% of gum mastic were placed between a microscope slide and a glass coverslip and melted on a Kofler bench at ca. 140 °C. The sample was rapidly cooled to room temperature. The coverslip was detached, and the powder of Form **IV** was carefully scraped with a needle. The powder was loaded into the Kapton 1.5 mm capillary and measured at 100 K using Oxford 700+ Cooler. The data collected on the two beamlines were in agreement, and data acquired on 11-BM did not add appreciably to the structure solution.

Computational Methods. CSP searches were performed using a rigid body random search algorithm in the UPACK program suite[32] with each molecule described using the general Amber force field (GAFF).[33] Atomic point charges for the classical force field were determined using the restricted electrostatic potential (RESP) charge assignment scheme[34] using RHF/6-31G*//MP2/6-31G* in Gaussian 09.[35] Individual searches were performed in parallel on selected space groups with a fixed number of molecules in the asymmetric unit (Z'). Z' = 1 structure searches included the space groups *Iba*2, *C*2, $C222_1$, *C*2/*c*, *Cc*, $P\bar{1}$, *P*1, $P2_1$, $P2_12_12$, $P2_12_12_1$, $P2_1/c$, *P*222, $P222_1$, *P*2/*c*, *Pba*2, *Pbca*, *Pbcn*, *Pc*, $Pca2_1$, *Pccn*, and $Pna2_1$. The Z' = 2 searches were performed for the space groups *C*2/*c*, *Cc*, $P\bar{1}$, $P2_1$, $P2_12_12$, $P2_12_12_1$, $P2_1/c$, *Pc*, $Pca2_1$, and $Pna2_1$. The space groups tested are the most commonly occurring space groups for molecular crystals in the Crystal Structure Database. At least 500 structures were generated in each search, with up to 50 000 candidate structures generated for some space groups. This collection of structures was then subject to similarity clustering and flexible molecule optimization routines, resulting in 2551 unique crystal structures within 40.0 kJ/mol of the

https://dx.doi.org/10.1021/acs.cgd.0c00096
Cryst. Growth Des. 2020, 20, 2670−2682

lowest energy form. A summary of the CSP results and the resulting energy vs molecular volume plot highlighting the relevant predicted forms are provided in Figure S4.

DFT optimizations were run in CP2K v. 2.6.2[36] using the Gaussian and plane wave (GPW) scheme[37] of the QUICKSTEP package.[38] In the first phase, cells were optimized with a cutoff of 450 Ry, the PBE exchange-correlation functional,[39] and the DZVP-MOLOPT-GTH (m-DZVP) basis set[40] paired with the appropriate dual-space GTH pseudopotentials.[41,42] All supercells were at least 10 Å on all sides. In the second optimization phase, the D3(BJ) dispersion correction[43,44] with a cutoff of 20 bohr was included and energies were evaluated using the TZVP-MOLOPT-GTH (m-TZVP) basis set, with the corresponding GTH pseudopotentials.[41,42] The SCF convergence threshold was 1×10^{-7} hartree using a fine integration grid and the following QUICKSTEP variables: 5 grids with a cutoff of 900 Ry and a relative cutoff of 70 Ry, EPS_RHO = 1×10^{-12}, EPS_PGF_ORB = 1×10^{-7}. The space group for each optimized structure was determined using PLATON.[45]

Diffuse-PXRD and (*h*0*l*) projections were calculated from our 20 × 20 × 1 unit cell atomistic crystal disorder models using the respective programs, DISCUS[46] or DIFFUSE.[47] Each short-range order (SRO) model output was controlled using the stochastic structure generator methods available in the program ZMC.[48] Other *ad hoc* computational scripts were used to read in relevant preliminary crystal structure coordinates and then create the multiple coordinate "building-block" sets necessary as separate input files for the ZMC program. The powder module in DISCUS was run in complete integration mode using the pseudo-Voigt peak shape function with profile parameters *u*, *v*, and *w* set to 0.0, 0.0, and 0.002. A Lorentz correction parameter was manually adjusted to 13.27, and the *hkl* grid was evenly spaced at 1.00 reciprocal lattice units (r.l.u.). All other parameters are default. The *h*0*l* diffraction section was calculated by averaging "total" scattering intensities over 2 lots that comprised 10 × 10 × 1 unit cells.

The interface energies were calculated by building two blocks of each structure (6 × 3 × 6 unit cells for $P2_12_12$ structures, 6 × 2 × 6 unit cells for *ac* interfaces of *Fdd*2 structures, and 3 × 2 × 10 unit cells for *bc* interfaces of *Fdd*2 structures), which were combined to create smooth interfaces. The energies of such structures, E_{mix}, were calculated under 3D periodic boundary conditions. Optimization and MD simulations were performed using LAMMPS (Large-scale Atomic/Molecular Massively Parallel Simulator) with the same GAFF parameters used for CSP. All the MD simulations were 3 ns and were performed in the NPT_F (constant particle number, pressure, temperature with flexible cells) ensemble at 300 K and 1 atm with a 1 fs time step. The energy values for each block and the combinations were averaged over the last 500 frames. The energies of corresponding bulk $P2_12_12$ and *Fdd*2 structures (E_{bulk}) were calculated in the same way. The interface energies were calculated as $E_{interface} = (E_{mix} - E_{bulk})/A$, where *A* is the area of the inteface. Since the energies of superimposed structures evaluated are the same (only their configurations or orientations were different), there was no need to calculate energies for each of two original building blocks.

The crystal-adiabatic free energy dynamics (C-AFED) simulations were run for 0.5 ns using a modified version of the MD code platform PINY_MD.[31] Simulation sizes were 4 × 2 × 8 unit cells (corresponding with *a*, *b*, and *c*) for the $P2_12_12$ and $P2_12_12_1$ structures (2 × 1 × 8 unit cells for the *Fdd*2), which produced a nearly cubic cell and total of 8192 atoms. Prior to the C-AFED run, each system was subject to energy optimization, as well as consecutive NVT and NPT_F equilibrations at 300 K for 20 ps. The time step for all MD runs was 0.5 fs. The C-AFED cell thermostat temperature was 200 000 K with the "mass-like" τ parameter set at 1000 fs.

RESULTS AND DISCUSSION

Crystallization and Thermotropic Behavior. Melt crystallization is a powerful method for polymorph discovery as it creates conditions far from equilibrium, yet results in slow growth and nucleation. This has been demonstrated by our identification of new polymorphs grown from the melt for a wide range of materials, including paracetamol,[49] testosterone propionate,[50] aspirin,[51] coumarin,[52] resorcinol,[53] and DDT.[54] Crystal growth under nanoconfinement also has been used for the discovery and stabilization of metastable forms,[55−60] wherein polymorph stability rankings deviate from bulk (unconfined) behavior.[61]

Rapid cooling of a benzamide melt with gum mastic to room temperature (ca. 20 °C) yielded two kinds of spherulites with distinct morphologies (Figure 1). Powder X-ray diffraction and

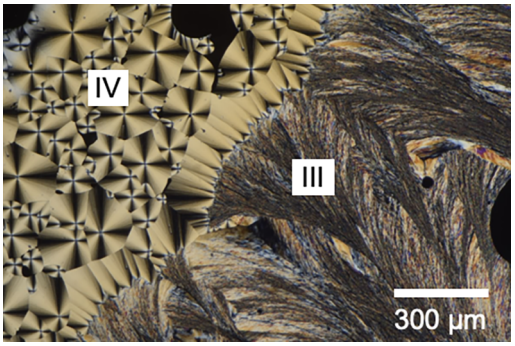

Figure 1. Polarized light optical micrograph of benzamide Forms **III** and **IV** spherulites grown by melt crystallization at room temperature with gum mastic (ca. 20 wt %).

Raman spectroscopy revealed that one of these morphologies corresponded to Form **III**, as deduced from comparison with published and newly collected data for Forms **I**, **II**, and **III**.[11] The other morphology, consisting of optically positive spherulites (large refractive index is radial), afforded a distinct PXRD pattern and Raman spectrum, supporting the formation of a new Form **IV** (Figure 2, see Figure 4B). Transformation of Form **IV** to Form **III** occurred within minutes at room temperature and significantly faster at elevated temperatures, precluding the determination of the melting temperature of Form **IV**. Crystallization of Form **IV** from the melt is more preferred in the presence of natural resins such as Canada balsam or gum mastic (ca. 20 wt %), which also slows the transformation to Form **III**. A reduction in phase transformation rates in the presence of resins and polymers, which has been well established for molecular crystals, can be attributed to slower diffusion and reduced growth of the transformation front.[51,52] When the benzamide−resin mixtures are confined between two glass slides, the transformation to Form **III** can take as long as several days, whereas unconfined benzamide−resin powders transform within hours. Form **IV** held at $T > 70$ °C for a few minutes transforms into **Form III**, even in the presence of resins (Figure 3).

Crystallization under confinement in various nanoporous media often results in changes in polymorph stability rankings and discovery of new polymorphs.[55−58] The crystallization of benzamide was examined using controlled pore glass (CPG) beads with nominal pore sizes of 4, 8, 35, 50, 100, and 200 nm after infiltration of benzamide melt. PXRD of benzamide confined in CPG beads with pore sizes $d \geq 35$ nm revealed 2θ peaks corresponding to the 011, 013, and 102 reflections of Form **III** (2θ = 16.5, 19.9, and 20.9°, respectively, Figure 4). The diffraction peaks for the benzamide crystals embedded in 8 nm pores, however, differ from those observed in the larger pore sizes, exhibiting unique reflections at 11.4, 18.9, 19.5, and 22.5° that correspond to the new Form **IV** observed from melt

https://dx.doi.org/10.1021/acs.cgd.0c00096
Cryst. Growth Des. 2020, 20, 2670−2682

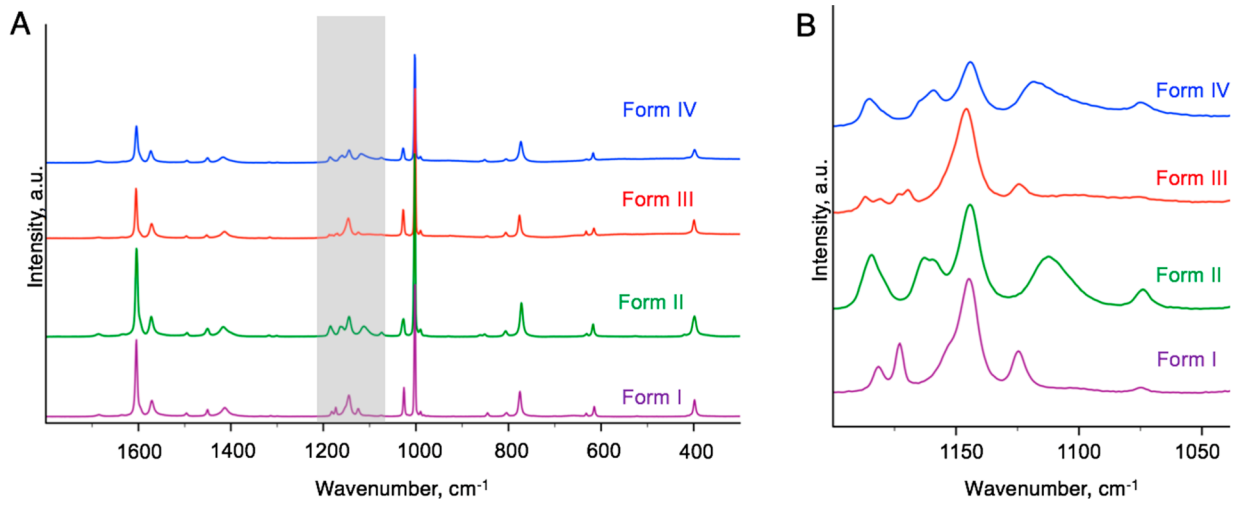

Figure 2. (A) Raman spectra of the four benzamide polymorphs. (B) Spectra in shaded region of A from 1200−1050 cm^{-1} enlarged.

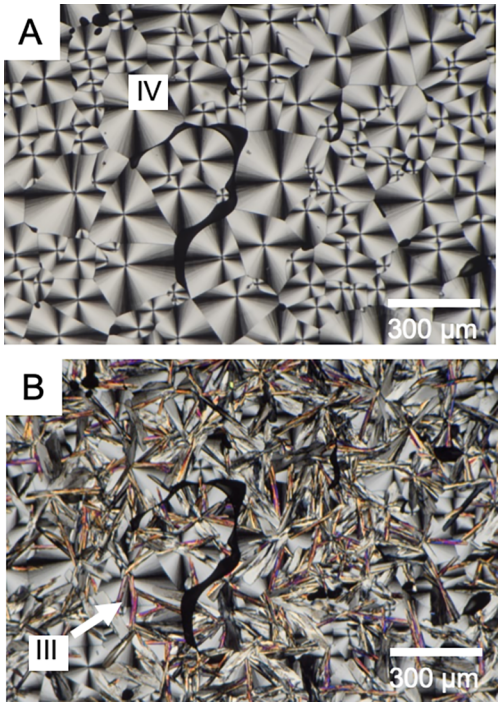

Figure 3. (A) Spherulites of Form **IV** grown by melt crystallization at room temperature in the presence of gum mastic (ca. 20 wt %). (B) Partial phase transformation of Form **IV** to Form **III** after raising the temperature to ca. 70 °C for less than 1 min.

crystallization. Numerous reports[55−57] have demonstrated Debye−Scherrer broadening for *hkl* reflections corresponding to planes about the zone axis parallel to the pore walls, which can lead to low peak intensities. Moreover, scattering from nanoscale crystals tends to be weak, with broad peaks, which can mask the peaks at 15 and 26° expected from the data for melt crystallization samples. The region near 6° likely indicates the presence of some Form **II** (admixed with Form **IV**), which is structurally similar to Form **IV**. Stronger peaks elsewhere, however, support Form **IV** as the dominant phase. Under ambient temperature and humidity, confined Form **IV** has remained stable for more than a year, in contrast to bulk Form **IV** that transforms to Form **III** within minutes. Benzamide confined in 4 nm pores does not crystallize even at elevated temperatures below the expected melting temperature for crystals of this size (see below).

The melting temperature of benzamide confined in CPG decreases with decreasing pore size, a direct consequence of the increasing surface-to-volume ratio when crystal size is reduced.[62,63] The melting point depression can be expressed according to a modified form of the Gibbs−Thomson equation[64−66] (eq 1), where ΔT_m is the melting point depression, $T_{m,bulk}$ is the bulk melting temperature, $T_m(d)$ is the melting temperature of the confined crystal with a diameter d (assumed to be of equivalent size to the host pores), $\Delta H_{fus,bulk}$ is the enthalpy of fusion, ρ_{solid} is the density of the solid, $\gamma_{crystal-melt}$ is the crystal−melt interfacial energy, and cos θ is the contact angle between an emerging spherical crystal and the pore wall (or any phase that may have wetted the pore wall).

$$\Delta T_m = T_{m,bulk} - T_m(d) = -\frac{4T_{m,bulk}\gamma_{crystal-melt}}{d\Delta H_{fus,bulk}\rho_{crystal}} \cos\theta \quad (1)$$

The Gibbs−Thomson equation often is simplified by assuming the contact angle θ = 180° (eq 2).

$$\frac{T_{m,bulk} - T_m(d)}{T_{m,bulk}} = \frac{4\gamma_{crystal-melt}}{d\Delta H_{fus,bulk}\rho_{crystal}} \quad (2)$$

Both eqs 1 and 2 predict a linear relationship between the melting point depression and the inverse of the crystal size. Using the enthalpy of fusion measured for bulk Form **III** ($\Delta H_{fus,bulk}$ = 159.4 J/g) and the density of Form **III** ($\rho_{crystal}$ = 1.28 g/cm^3), the slope of T_m vs. $1/d$ gives $\gamma_{crystal-melt}$ = 40.8(1.1) mJ/m^2. To evaluate the validity of the interfacial energy obtained, we consider the lower limit of the crystal-melt interface energy, which can be estimated from a semiempirical model[67] (eq 3).

$$\gamma_{crystal-melt} = \frac{3}{8}\frac{RT_{m,bulk}}{N_A^{1/3}\omega^{2/3}} \exp\left(\frac{\Delta H_{fus,bulk}}{3RT_{m,bulk}}\right) \quad (3)$$

Here, R is the universal gas constant, N_A is the Avogadro number, and ω = 90.4 cm^3/mol is the benzamide molar volume. An estimation of the surface free energy from bulk properties, as in eq 3, gives $\gamma_{crystal-melt}$ = 50.7 mJ/m^2, which agrees surprisingly well with the experimental values obtained

https://dx.doi.org/10.1021/acs.cgd.0c00096
Cryst. Growth Des. 2020, 20, 2670−2682

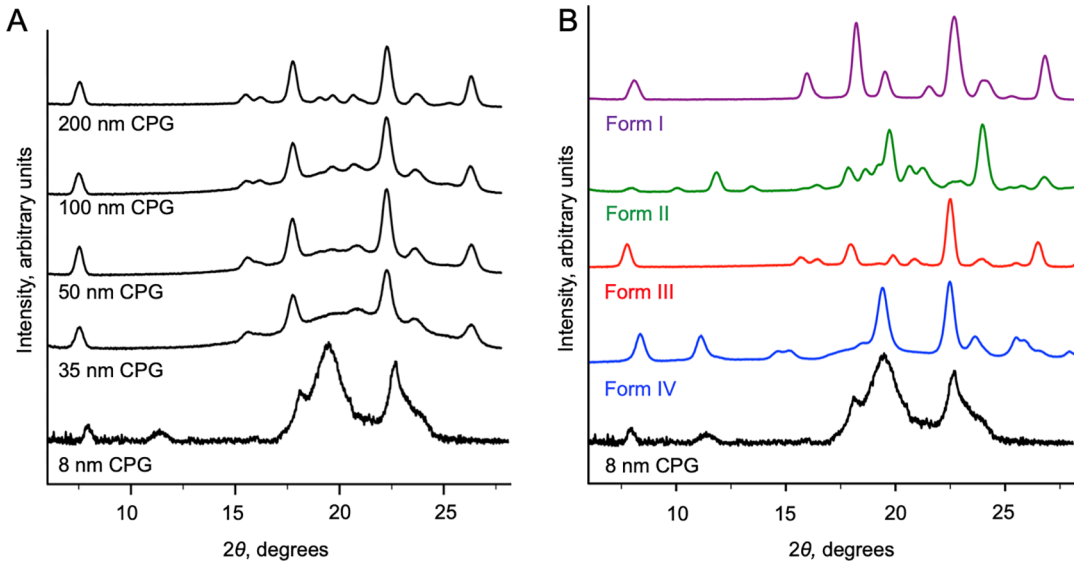

Figure 4. (A) PXRD data for benzamide nanocrystals embedded in CPG. (B) Comparison of benzamide PXRD data in 8 nm pores with bulk **I**, **II**, **III**, and **IV** phases.

by DSC and interface energy calculations above. This correspondence argues that the assumption of a contact angle $\theta = 180°$ between the confined nanocrystals and the pore walls is reasonable. We note, however, that contact of the confined nanocrystals with an intervening amorphous phase lining the pore walls cannot be discounted.[68] Controlled pore glass beads used in confinement experiments have hydrophilic surfaces and are likely wetted by benzamide, suggesting that the crystals inside pores are separated from the walls by an amorphous benzamide layer. Ultimately, extrapolation of the data for Form **III** in Figure 5 to 8 nm pore size ($1/d = 0.125$ nm^{-1}) indicates a melting point of 88.3 °C. This value is substantially higher than the actual measured value in 8 nm pores, corroborating the crystallization of the less stable Form **IV**.

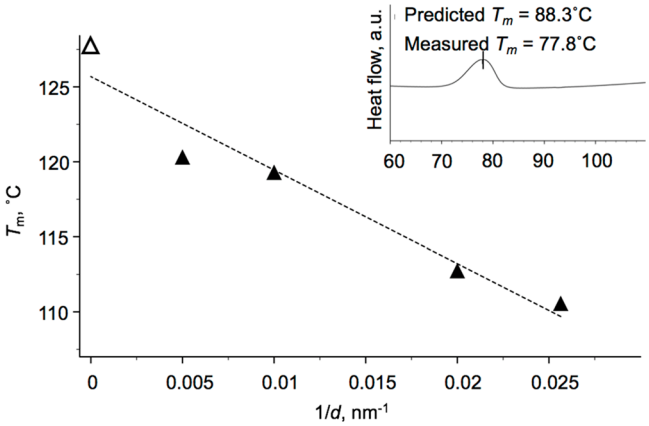

Figure 5. Dependence of the melting temperature, T_m, on the inverse of the pore diameter, $1/d$, for benzamide Form **III**. The diameters correspond to the nominal CPG pore sizes. The contact angle θ in eq 1 is assumed to be 180°. The dashed lines represent the best linear fit to the data set. $T_{m,bulk}$ is denoted as the open triangle. Inset: DSC heating scan for benzamide confined in 8 nm pores.

PXRD Data Analysis of Form IV. While polycrystalline samples of Form **IV** were obtained from the melt and through nanoscale confinement, single crystals could not be obtained. Moreover, the PXRD data collected on the GADDS microdiffractometer (Figure 4 and Figure S1) was not sufficient for structure determination. Therefore, structure analysis was performed using synchrotron powder data recorded at the 17-BM beamline (λ = 0.45212 Å, Advanced Photon Source, Argonne National Laboratory). A two-dimensional pattern collected did not exhibit texture (inset in Figure 6), indicating a polycrystalline sample with no preferred orientation. The powder X-ray diffraction (PXRD) pattern (Figure 6), indexed with the software McMaille v3.04,[69] was consistent with an orthorhombic unit cell (a = 11.83 Å, b = 20.50 Å, and c = 5.03 Å). A Pawley fit of the data in the space group $P2_12_12_1$ afforded R_{wp} = 5.99%. The hkl reflections with $l \neq 0$ were broad and weak, however (Figure S2). A Pawley fit of similar quality (R_{wp} = 7.1%) was obtained using only $hk0$ reflections (with c set to 0.1 Å in the Pawley fitting). Additional high-resolution synchrotron measurements of Form **IV** were recorded at 11-

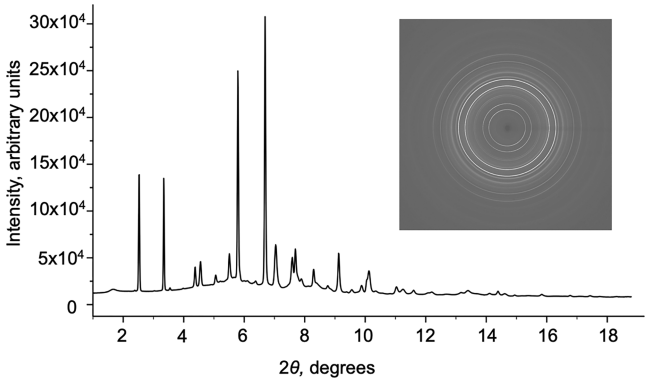

Figure 6. Synchrotron powder diffraction data of benzamide Form **IV** collected at 17-BM beamline of the Advanced Photon Source, Argonne National Laboratory, at a wavelength of 0.45212 Å and temperature of 100 K. Insert: 2D diffraction pattern used to make 1D intensity vs 2θ plot. Continuous Debye−Sherrer diffraction rings without discrete diffraction spots are consistent with the absence of texture.

https://dx.doi.org/10.1021/acs.cgd.0c00096
Cryst. Growth Des. 2020, 20, 2670−2682

Table 1. DFT-Optimized Unit Cell Parameters and Relative Lattice Energies for the Candidate Form IV Structures, As Well As Structures Determined by Optimization of the Reported Structures of Forms I, II, and III

generation method[a]	initial space group	final space group	E (kJ/mol)	Z'	a (Å)	b (Å)	c (Å)	β (deg)	outcome
I (optimized BZAMID02)	$P2_1/c$	$P2_1/c$	0.00	1	5.551	5.010	21.216	91.22	benzamide **I**
III (optimized BZAMID12)	$P2_1/c$	$P2_1/n$	0.23	1	5.039	5.449	21.575	90.04	benzamide **III**
SA	$P2_1/c$	$P2_1/n$	2.52	2	5.249	17.753	13.117	96.49	unit cell of **II**[b,c]
II (optimized BZAMID13)	$Fdd2$	$Fdd2$	2.78	2	33.856	27.994	5.170	90	benzamide **II**
SA	$Pnn2$[d]	$Fdd2$	4.48	2	23.303	40.481	5.166	90	possible **IV**
CSP	$P2_12_12_1$	$P2_12_12_1$	4.68	2	5.072	11.405	20.955	90	possible **IV**
CSP	$P2_1/c$	$P2_1/c$	6.20	2	5.173	15.923	15.150	98.15	unit cell does not fit
CSP	$P2_1/c$	$P2_1/n$	7.44	2	5.157	20.880	11.561	99.37	possible **IV**
CSP	$P2_12_12$	$P2_12_12$	8.21	2	12.435	19.785	5.162	90	possible **IV**
SA	$Pna2_1$	$Pna2_1$	8.98	2	14.421	16.935	5.149	90	unit cell of **II**[c]
SA	$P2_12_12_1$	$P2_12_12_1$	9.37	2	5.228	10.230	23.615	90	unit cell does not fit
CSP	$Pna2_1$	$Pna2_1$	10.24	2	17.394	14.923	5.001	90	unit cell of **II**[c]
SA	$P2_1/n$	$P2_1/c$	10.84	2	5.020	24.174	11.086	102.21	unit cell does not fit

[a]Structure generation methods: SA, simulated annealing; CSP, crystal structure prediction. [b]Corresponds to the predicted structure #22 in ref 15. [c]2D lattice parameters in the optimized structure are twice the values of those in SA and CSP structures. [d]With force field, optimized as $P1$ (Table S3).

BM beamline (λ = 0.412827 Å, Advanced Photon Source, Argonne National Laboratory). Despite higher angular resolution, no additional information was obtained because of significant peak broadening (Figure S3). Similarities in the two measurements imply disorder that is inherent in the benzamide crystal, which allows extraction of only 2D data. Nevertheless, candidate structures for benzamide Form **IV** can be found using the 2D data.

Structure Generation. Pawley fits for all orthorhombic and monoclinic space groups (γ = 90° while α or β can deviate from 90° due to uncertainty in c orientation) were evaluated using $hk0$ reflections (c = 0.1 Å). The $P2_12_12_1$, $P2_12_12$, $Pna2_1$, $Pba2$, $Pbn2_1$, $Pnn2$, $Pbam$, $Pnnm$, $Pbnm$, $Pnam$, $P2_1/b$, $P2_1/n$ space groups provided reasonable fits ($R_{wp} \leq 8\%$). These space groups were then used to generate structure solutions by simulated annealing (SA) in Bruker TOPAS 4 software.[70] The geometry of each molecule was defined as a rigid body based on Form **I** atomic coordinates, and rotational and translational parameters were simultaneously refined during SA search. Due to the severe disorder, only $hk0$ reflections were used to compare simulated and observed PXRD data. Six structures with the best $R_{wp} \leq 12\%$ were selected for further computation analysis (SA entries in Table 1 and Table S2). Because simulated annealing did not produce an obvious structure solution, crystal structure prediction (CSP) was employed to generate alternative candidates. Random structures were generated with the UPACK program suite[71] using the general Amber force field (GAFF).[72] Candidate structures were filtered by identifying all matches with CSP-generated unit cells against the indexed parameters of the possible 2D cell for Form **IV** (within a 5% tolerance; for CSP details, see the Computational Methods section). Five structures of the 34 cells that matched the experimentally determined 2D unit cell parameters (Figure S4) had simulated PXRD patterns with low angle 2θ values and intensities consistent with the experimental data for Form **IV**.

All 11 Form **IV** candidate structures generated by SA and CSP were ranked by optimizing their structures with density functional theory (DFT). Forms **I**, **II**, and **III** also were optimized for comparison (CSD ref codes: BZAMID02 BZAMID13, and BZAMID12 respectively). Structures of Form **IV** generated by simulated annealing were first optimized using the GAFF force field embedded in the GULP software with preservation of their respective space group symmetries. The $Pba2$ and $Pnn2$ cells did not reach minimum energy structures unless optimized after the symmetry was reduced to $P1$. Both the transition state (full symmetry) and local minimum ($P1$) cells were included as candidate forms. The eight structures from simulated annealing and five structures from CSP were subsequently optimized without space group symmetries using DFT calculations in CP2K v. 2.6.2[36] (see the Computational Methods section for details). The three structures that optimized to $P1$ cells with Z' = 8 are not reported in Table 1 (see Table S3); these include the two saddle point structures from simulated annealing ($Pba2$ and $Pnn2$) and the $Pba2$ structure optimized as $P1$ using the classical force field. Optimized structures with unit cells that differed by more than 10% from the experimental 2D lattice parameters were excluded as Form **IV** candidates. Curiously, three structures optimized to unit cells that resembled the reported $Fdd2$ structure of Form **II**[15] as well as its optimized version (Table 1), suggesting that Forms **II** and **IV** are similar. Consequently, the set of DFT optimized structures (Table 1, Figure 7) was narrowed to four potential candidates for Form **IV**: $Fdd2$ (4.48 kJ/mol), $P2_12_12_1$ (4.68 kJ/mol), $P2_1/n$ (7.44 kJ/mol), and $P2_12_12$ (8.21 kJ/mol).

Description of Candidate Structures. The four aforementioned candidate structures adopt a parquet-like motif of tiles, each consisting of a tetrad of benzamide molecules, stacked normal to the 5 Å axis. The tiles are parallelograms with nearly the same dimensions; the length of one side approximately twice the length of the other, $l = 2w$, and an angle ϕ between the two sides (Figure 8). The tetrads in the candidate Form **IV** structures resemble those in Form **II**,[8,15] but the tiles have different dimensions (w = 7.8 Å and ϕ = 82° in Form **IV** vs w = 8.3 Å and ϕ = 63° in Form **II**). Unlike Forms **I** and **III**, in which benzamide molecules are associated by hydrogen-bonded $R_2^2(8)$[73] dimers that assemble further through dimeric hydrogen-bonded $R_4^2(8)$ tapes, Form **IV** forms skewed $R_3^2(8)$ rings from three benzamide molecules that assemble into a hydrogen-bonded $R_3^2(8)$ catemeric tape (Figure 9). Candidate structures with the $R_2^2(8)$ dimers observed in Forms **I** and **III** resulted in optimized unit cells that did not correspond with the PXRD cell of experimental

https://dx.doi.org/10.1021/acs.cgd.0c00096
Cryst. Growth Des. 2020, 20, 2670−2682

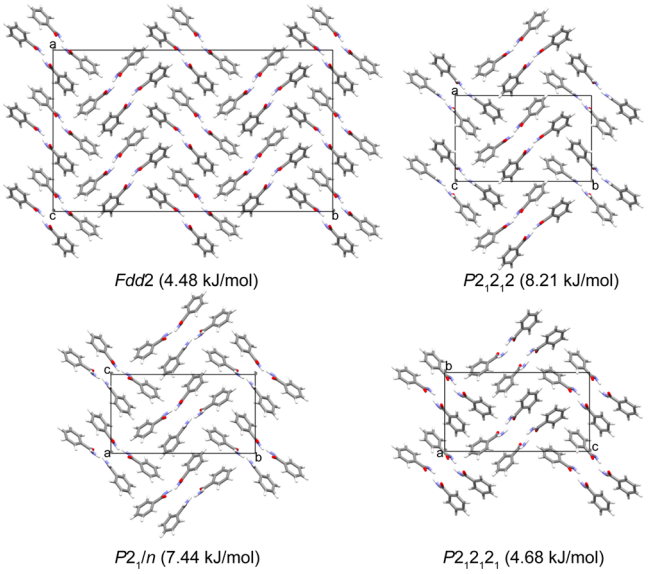

Figure 7. Four candidate Form **IV** structures. All four structures consist of benzamide tetrad tiles that stack along the short 5 Å axis (normal to the plane of the page) through catemeric hydrogen-bonds. With the exception of $P2_1/n$ structure, all the carbonyls within a tile point in the same direction. The energy values for each structure are relative to optimized Form **I** (Table 1).

Form **IV** (Table S4). One of the *P*1 structures (Table S4, 7.90 kJ/mol) does contain $R_2^2(8)$ dimers but is unlikely because $Z' = 8$.

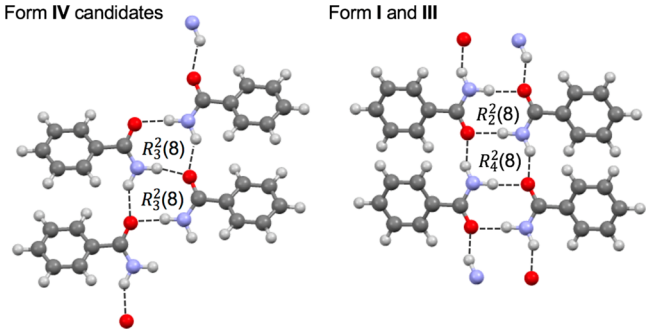

Figure 9. Hydrogen-bonding motifs for Form **IV** candidate structures (left) and Forms **I** and **III** (right). Graph set notations are indicated.

All four candidates of Form **IV** contain three types of phenyl−phenyl contacts within the tetrads and between tetrads. T- and E-contacts describe interactions between neighboring tiles (Figure 8). T-contacts, in which a (phenyl) C−H bond points toward a phenyl ring on a neighboring tetrad,[74,75] occur in all candidate structures and are characterized by dihedral angles of 68−78°. External contacts, E, between parallel tiles associate in two motifs. V-contacts (for the V-shaped geometry of the two neighboring rings) adopt an edge-to-face herringbone arrangement, with dihedral angles E_V = 67−72° between neighboring phenyl rings. P-contacts (for the parallel arrangement of two neighboring rings) exhibit dihedral angles E_P = 0−7°. I-contacts describe phenyl ring associations within a tile (Figure 8). *Fdd*2 and $P2_12_12$ belong to one family with internal V-contacts, characterized by

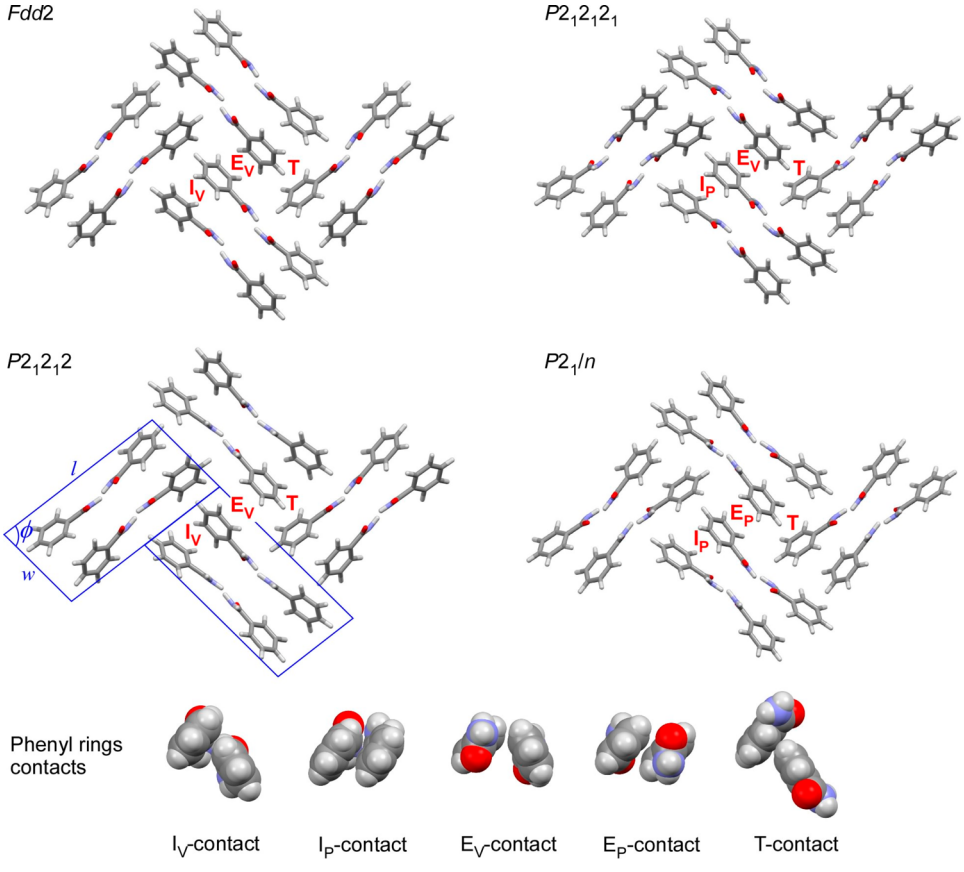

Figure 8. Molecular packing of the tetrads in the four Form **IV** candidate structures.

https://dx.doi.org/10.1021/acs.cgd.0c00096
Cryst. Growth Des. 2020, 20, 2670−2682

dihedral angles of I_V = 67−69°. In contrast, $P2_12_12_1$ and $P2_1/n$ form a second family of structures, all with nearly parallel phenyl rings (P-contact) with corresponding dihedral angles I_P = 10−11° (Table S5).

The two families of candidates were evaluated by Rietveld refinement using the DFT-determined structures of Form **IV**. Although the R_{wp} values of all four structures were high, the structures with the I_V-contacts (*Fdd*2, $P2_12_12$; Figures 7, 8) exhibited the best fits (R_{wp}) to the experimental data, suggesting this type of tile is more likely than I_P-contacts in Form **IV**. Although the comprehensive analysis described above narrows the choice to two structures consistent with experimental 2D data, the poor fits to the experimental 3D PXRD data (Figure S5), which are a consequence of the weak reflections for *hkl* where $l \neq 0$, argues for severe disorder along the short 5 Å axis. *Fdd*2 and $P2_12_12$ structures exhibit internal V-contacts.

Interface Energies. A high degree of disorder suggests the existence of randomly distributed nanoscale domains, corresponding to one or several tiles, which warrants consideration on the role of interface energy on developing a model structure. The $P2_12_12$ structure is enantiomorphous, whereas the *Fdd*2 structure is polar (Figure 10). It is unlikely that

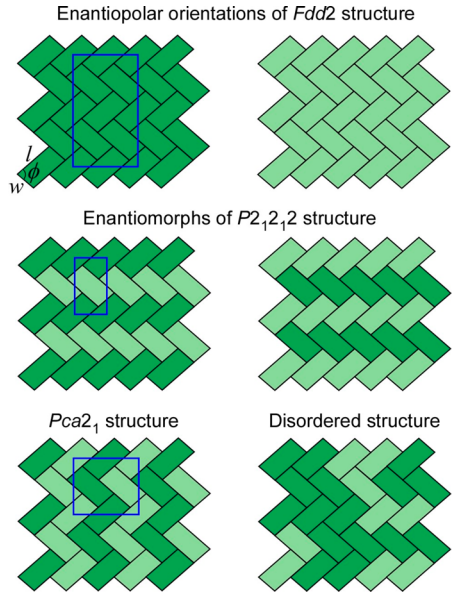

Figure 10. Idealized tiling motifs for internal V-contact structures *Fdd*2 and $P2_12_12_1$ (with enantiomorphs), $Pca2_1$, and an example of a disordered structure. Unit cells are outlined in blue. Dark and light green tiles represent tetrads of benzamide molecules in which all the C−O vectors are pointing out of and into the page, respectively. These schemes do not distinguish the relative shifts of catemers normal to the page.

disorder would result from random mixtures of 2D layers in which the carbonyls are pointing in different directions, as this would cut the catemeric chains. Instead, disorder is better represented by the schemes in Figure 11, which describe domain boundaries along the *ac* and *bc* planes for both structures. Enantiomorphs of $P2_12_12$ are distinguished by subscripts *p* and *q*. The *Fdd*2 structure, with the polar axis pointing in enantiopolar directions, is distinguished as *u* and *d* (carbonyls up and down). There are an indefinite number of ways to arrange the tetrads into nanoscale domains of various sizes and symmetries. One particularly interesting example that effectively combines the tiling pattern of *Fdd*2 and $P2_12_12$ is a low energy (8.30 kJ/mol relative to Form **I**) orthorhombic $Pca2_1$ structure with Z' = 4 and I_V-contacts as well (Figure S6). This structure results in different domain interfaces.

The energies of the interfaces between the nanoscale domains were calculated by molecular dynamic (MD) simulations that combine two enantiomorphic or enantiopolar building blocks. The corresponding energies of the bulk structures (see the Experimental Section and Figure 11) were compared. The calculated interface energies were comparable (Table 3) to the surface energies determined for crystal−melt interface energies of ca. 41 mJ/m^2 obtained from the DSC data on crystallization in confinement (see above).

Disorder Model. Distinct peaks associated with *hkl* reflections for $l \neq 0$ are absent in the experimental PXRD pattern. The *hk*1, *hk*2, and *hk*3 Bragg reflections, expected at $2\theta < 18°$, were effectively extinct, which can be a signature of a 2D-stacking fault disorder. Using atomistic models, it is possible to simulate the disorder among neighboring stacks of tiles and the associated PXRD patterns. The *Fdd*2 structure consists of tiles in which the all carbonyl groups orient along the same direction, at 0, 1/4, 1/2, 3/4, parallel to the 5 Å tape axis. The $P2_12_12$ structure consists of the same tiles but with one-half of the carbonyl groups oriented up, at 0, 1/2, and the other half down, at 0, 1/2, with respect to the tape axis. Disorder models, each consisting of 20 × 20 × 1 supercell, were built from random combinations of single stacks corresponding to the *Fdd*2 and $P2_12_12$ structures and PXRD pattern generated using ZMC and DISCUS[46,76] software suites (see the Computational Methods section for details) and then were compared to the experimental pattern. It is important to note that a random collection of *Fdd*2-like all "up" and all "down" tapes (where up and down denote the direction of the carbonyl groups), combined with translations of 0, 1/4, 1/2, 3/4 along the tape axis, is indistinguishable from a random arrangement of $P2_12_12$-like tapes. Three possible settings were used to characterize the disorder using the *Fdd*2-like tapes only: random tape orientation (C1), random tape displacements (in increments of 1/4) along the short axis (C2), and both (C3). Figure 10 depicts the random distribution of orientations (random tape displacements cannot be discerned from this figure). This kind of analysis is commonly used for the interpretation of single crystal X-ray diffuse scattering or pair distribution functions.[48,77]

Although the choices for the candidate structures were narrowed to *Fdd*2 and $P2_12_12$, both with I_V contacts, disorder models were also built from the tiling in the $P2_12_12_1$ and $P2_1/n$ structures, which have I_P contacts to confirm that the former pair represented the best candidate structures. Pattern B in Figure 12 corresponds to the I_P model with both random orientations and displacements. Comparison with the Form **IV** experimental data (pattern A) shows significant disagreements in peak intensities. The diffuse scattering calculated at $2\theta \sim 5°$ for I_P models is not apparent in the experimental data, thus arguing against the two I_P candidates ($P2_12_12_1$, $P2_1/n$; Figure 7).

Inspection of the PXRD patterns (Figure 12) calculated for the aforementioned disordered I_V models C1, C2, and C3 reveals distinct differences. The random tape orientations in the C1 model do not extinguish *hkl* reflections adequately for $l \neq 0$, as evidenced by peaks in the C1 pattern that are not observed in the experimental data (e.g. peaks at 2θ = 6.1, 6.5, 8.4°). C2, with random tape displacements, and C3, with both

https://dx.doi.org/10.1021/acs.cgd.0c00096
Cryst. Growth Des. 2020, 20, 2670−2682

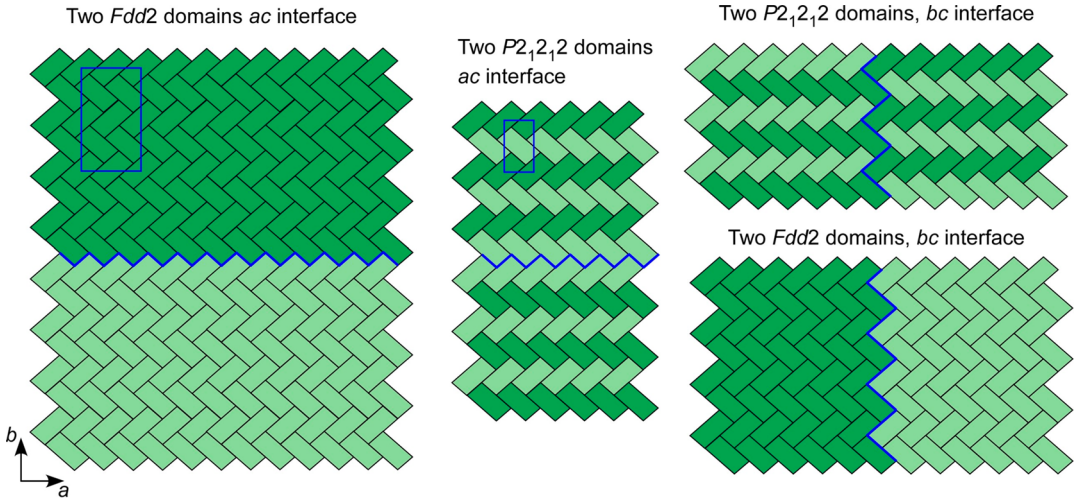

Figure 11. Supercells used to calculate the interface energies. Unit cells of $P2_12_12$ and *Fdd*2 structures are outlined in blue. Calculated interfaces are indicated in blue. Dark and light green tiles represent tetrads of benzamide molecules in which all oxygens from amino groups are pointing out of and into the page, respectively.

Table 3. Interface Energies ($E_{interface}$) for Combinations of Enantiomorphic and Enantiopolar Domains of Most Probable Crystal Structure Candidates (Figure 11)

building blocks	interface plane	interface structure	$E_{interface}$, mJ/m^2
$(P2_12_12)_p + (P2_12_12)_q$	*ac*	*Fdd*2	34
	bc	$Pca2_1$	12
$(Fdd2)_u + (Fdd2)_d$	*ac*	$P2_12_12$	140
	bc	$Pca2_1$	50

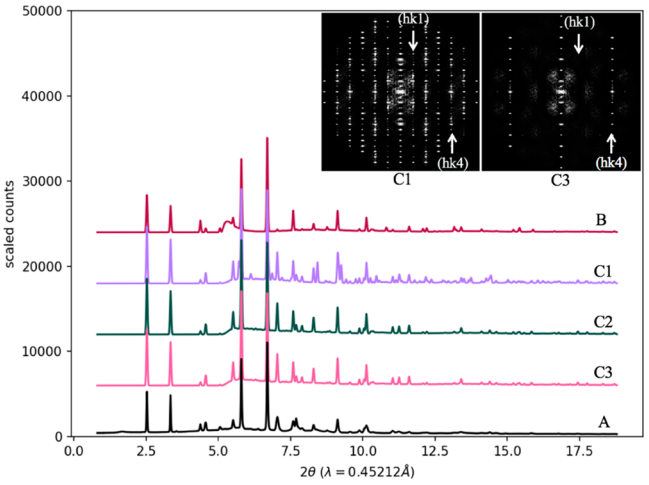

Figure 12. Comparison of calculated PXRD from 2D-disorder models and analogous (*h*0*l*) sections demonstrating the effect on diffraction from structures with and without random displacements of neighboring tiles. (A) Observed data. (B) Calculated PXRD from a random displacement-orientation model with I_P-contact tiles. (C) Calculated diffraction patterns from models where tiles are all I_V-contact, adopting random orientation disorder (C1) or displacement disorder (C2) or both (C3).

random tape displacements and orientations, extinguish the *hk*1, *hk*2, and *hk*3 Bragg reflections, similar to the experimental PXRD data. The extinction of *hk*1, *hk*2, and *hk*3 reflections also can be validated from the corresponding reciprocal space sections for C1 and C3 calculated using DIFFUSE[47] (Figure 12). Collectively, these observations demonstrate that disorder of the tape orientations alone is not sufficient to explain the observed data.

Crystal Adiabatic Free Energy Dynamics (C-AFED) Analysis. The PXRD data is consistent with the presence of 2D disorder in Form **IV**, explained further through modeling as related to displacement of the tapes along the short stacking axes. This does not imply that a mechanical crystal distortion allows tiles to slip past each other, as faults also could occur during crystal growth. Alternatively, disorder could reflect nearly equal energies for the possible domain boundaries between stacks of tiles.[78] One approach for testing the propensity of a structure to exhibit stacking faults is to simulate deformations using molecular dynamics (MD).[79] In particular, C-AFED simulations can accommodate unit cell fluctuations that might lead to disorder.[80,81]

Comparison of initial (after NPT_F equilibration) and final frames from 500 ps C-AFED simulations for *Fdd*2 and $P2_12_12$ are shown in Figure 13. The blue and red colors represent the magnitude of atomic *z*-displacements from the base of the simulation box. The *Fdd*2 molecules appear relatively unchanged in their positions between the first and final frames. In contrast, the $P2_12_12$ simulation shows clear fluctuations of the molecules along the *z*-displacement, as evidenced by the skewed stripes of color for molecules that started with the same *z*-displacement. This suggests that the $P2_12_12$ tiling can accommodate displacements more readily than the *Fdd*2 form. These stacking faults are consistent with the disorder models that best match the PXRD data. While the *Fdd*2 tiling is lower in energy and more structurally stable in the MD simulations, the lack of characteristic peaks in the PXRD data rules out domains larger than just a few tetrad tiles. Combining the SRO models with the MD results, we find that Form **IV** likely incorporates small *Fdd*2-type domains with varied orientations relative to their nearest neighbors, as shown by the disordered structure in Figure 10.

CONCLUSIONS

A new, highly metastable benzamide Form **IV** polymorph was discovered by melt crystallization in parallel with growth under nanoconfinement in very small pores. Under nanoscale confinement, the melting behavior of more stable benzamide

https://dx.doi.org/10.1021/acs.cgd.0c00096
Cryst. Growth Des. 2020, 20, 2670−2682

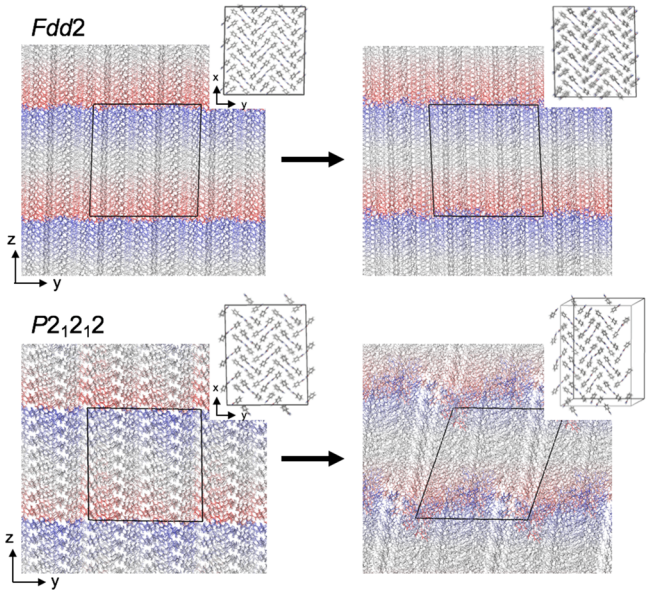

Figure 13. C-AFED simulations for two Form **IV** models, *Fdd*2 and $P2_12_12$. Large C-AFED simulation cells are viewed along the *y*-axis; the *z*-axis is vertical. Coloring (red → gray → blue) denotes the relative, periodic positions of the molecules in the initial frames on the left and the displacements on the right. Fluctuations in the positions of the $P2_12_12$ molecules are evidence of stacking faults. The insets correspond to *xy* sections viewed along the *z*-axis for each frame.

Form **III** crystallizing in larger pores was strongly influenced by the pore size, with the melting depression scaling inversely with crystal size. Interfacial energies calculated by the Gibbs–Thomson equation agreed with those obtained by semi-empirical model. Using a combination of powder X-ray diffraction analysis and computational methods, a large number of candidate structures for benzamide Form **IV** were reduced to a few possible disorder models based on tapes of 2D parquet-like tiles consisting of benzamide tetrads. The disorder could be explained by various stacking fault configurations corresponding to random tape displacements *and* orientations. Collectively, these observations reveal an impressive crystallographic complexity for such a simple molecule, yet one that is within reach of emerging methods for determination of solid-state structure. Moreover, this analysis suggests that many structures that may have been abandoned because of catch-all shortcomings, such as poor crystallinity, twinning, or disorder, can be solved.

■ ASSOCIATED CONTENT

Supporting Information

The Supporting Information is available free of charge at https://pubs.acs.org/doi/10.1021/acs.cgd.0c00096.

Tables of CPG pore manufacturer specifications, space groups selected, DFT-optimized unit cell parameters and relative lattice energies, hydrogen bonding and phenyl arrangement motifs, and structural parameters for candidate structures and figures of PXRD patterns, 17-BM beamline synchrotron diffraction data, comparison of synchrotron powder diffraction patterns, energy vs molecular volume plot, overlay of calculated PXRD patterns, and projections of structures (PDF)

Five hundred lowest energy structure from CSP (CIF)

Thirty-five 2D cells from the initial CSP search consistent with the experimental lattice parameters for *hk*0 indices (CIF)

Seventeen 3D structures CSP and simulating annealing corresponding to entries in Table 1 and Table S2 (CIF)

■ AUTHOR INFORMATION

Corresponding Authors

Alexander G. Shtukenberg − *Department of Chemistry and Molecular Design Institute, New York University, New York City, New York 10003, United States;* orcid.org/0000-0002-5590-4758; Email: shtukenberg@mail.ru

Mark E. Tuckerman − *Department of Chemistry and Courant Institute of Mathematical Science, New York University, New York City, New York 10003, United States; Center for Computational Chemistry at NYU Shanghai, New York University−East China Normal University, Shanghai 200062, China;* orcid.org/0000-0003-2194-9955; Email: mark.tuckerman@nyu.edu

Bart Kahr − *Department of Chemistry and Molecular Design Institute, New York University, New York City, New York 10003, United States;* orcid.org/0000-0002-7005-4464; Email: bart.kahr@nyu.edu

Michael D. Ward − *Department of Chemistry and Molecular Design Institute, New York University, New York City, New York 10003, United States;* orcid.org/0000-0002-2090-781X; Email: mdw3@nyu.edu

Authors

Noalle Fellah − *Department of Chemistry and Molecular Design Institute, New York University, New York City, New York 10003, United States;* orcid.org/0000-0002-5561-4064

Eric J. Chan − *Department of Chemistry, New York University, New York City, New York 10003, United States;* orcid.org/0000-0003-1105-2773

Leslie Vogt-Maranto − *Department of Chemistry, New York University, New York City, New York 10003, United States;* orcid.org/0000-0002-7006-4582

Wenqian Xu − *X-ray Science Division, Advanced Photon Source, Argonne National Laboratory, Argonne, Illinois 60349, United States*

Chao Li − *Department of Chemistry and Molecular Design Institute, New York University, New York City, New York 10003, United States*

Complete contact information is available at: https://pubs.acs.org/10.1021/acs.cgd.0c00096

Notes

The authors declare no competing financial interest.

■ ACKNOWLEDGMENTS

This work was supported by the National Science Foundation under award numbers DMR-1708716 and DMR-1608374 and the New York University Materials Research Science and Engineering Center (MRSEC) program of the National Science Foundation under award number DMR-1420073. The authors acknowledge Dr. Chunhua Hu (NYU Department of Chemistry X-ray Diffraction Facility), the NSF Chemistry Research Instrumentation and Facilities Program (CHE-0840277), and NSF MRSEC Program under award number DMR-0820341 for the powder microdiffractometer with GADDS. This work was supported by computational resources

https://dx.doi.org/10.1021/acs.cgd.0c00096
Cryst. Growth Des. 2020, 20, 2670−2682

provided by High Performance Computing at New York University. Use of the Advanced Photon Source at Argonne National Laboratory was supported by the U.S. Department of Energy, Office of Science, and Office of Basic Energy Sciences, under contract no. DE-AC02-06CH11357. We are grateful to Dr. Lynn W. Ribaud and Dr. Saul D. Lapidus for providing assistance in collecting synchrotron powder diffraction data at Advanced Photon Source. The authors thank Prof. Qiang Zhu for a preliminary crystal structure prediction search and Prof. Martin Schmidt for helpful discussions on benzamide structure.

REFERENCES

(1) von Liebig, J.; Wöhler, F. Untersuchungen über das radikal der benzoesäure. *Ann. Pharm.* **1832**, *3*, 249−282.
(2) Sonda, S.; Katayama, K.; Kawahara, T.; Sato, N.; Asano, K. Synthesis and pharmacological properties of benzamide derivatives as selective serotonin 4 receptor agonists. *Bioorg. Med. Chem.* **2004**, *12*, 2737−2747.
(3) Zhang, D.; Kohlman, D.; Krushinski, J.; Liang, S.; Ying, B.-P.; Reilly, J. E.; Dinn, S. R.; Wainscott, D. B.; Nutter, S.; Gough, W.; Nelson, D. L. G.; Schaus, J. M.; Xu, Y.-C. Design, synthesis and evaluation of bicyclic benzamides as novel 5-HT1F receptor agonists. *Bioorg. Med. Chem. Lett.* **2004**, *14*, 6011−6016.
(4) Suzuki, T.; Ando, T.; Tsuchiya, K.; Fukazawa, N.; Saito, A.; Mariko, Y.; Yamashita, T.; Nakanishi, O. Synthesis and Histone Deacetylase Inhibitory Activity of New Benzamide Derivatives. *J. Med. Chem.* **1999**, *42*, 3001−3003.
(5) Moradei, O. M.; Mallais, T. C.; Frechette, S.; Paquin, I.; Tessier, P. E.; Leit, S. M.; Fournel, M.; Bonfils, C.; Trachy-Bourget, M.-C.; Liu, J.; Yan, T. P.; Lu, A.-H.; Rahil, J.; Wang, J.; Lefebvre, S.; Li, Z.; Vaisburg, A. F.; Besterman, J. M. Novel aminophenyl benzamide-type histone deacetylase inhibitors with enhanced potency and selectivity. *J. Med. Chem.* **2007**, *50*, 5543−5546.
(6) Deffet, L. *Répertoire des Composés organiques polymorphes*, Éditions Desoer: Liége, Belgium, 1942.
(7) Penfold, B. R.; White, J. C. B. The crystal and molecular structure of benzamide. *Acta Crystallogr.* **1959**, *12*, 130−135.
(8) Blagden, N.; Davey, R.; Dent, G.; Song, M.; David, W. I. F.; Pulham, C. R.; Shankland, K. Woehler and Liebig revisited: A small molecule reveals its secrets the crystal structure of the unstable polymorph of benzamide solved after 173 years. *Cryst. Growth Des.* **2005**, *5*, 2218−2224.
(9) David, W. I. F.; Shankland, K.; Pulham, C. R.; Blagden, N.; Davey, R. J.; Song, M. Polymorphism in benzamide. *Angew. Chem., Int. Ed.* **2005**, *44*, 7032−7035.
(10) Thun, J.; Seyfarth, L.; Senker, J.; Dinnebier, R. E.; Breu, J. Polymorphism in benzamide: Solving a 175-year-old riddle. *Angew. Chem., Int. Ed.* **2007**, *46*, 6729−6731.
(11) Butterhof, C.; Martin, T.; Ectors, P.; Zahn, D.; Niemietz, P.; Senker, J.; Näther, C.; Breu, J. Thermoanalytical evidence of metastable molecular defects in form I of benzamide. *Cryst. Growth Des.* **2012**, *12*, 5365−5372.
(12) Benoit, D. M.; Ectors, P.; Duchstein, P.; Breu, J.; Zahn, D. A new polymorph (IV) of benzamide: structural characterization and mechanism of the I↔ IV phase transition. *Chem. Phys. Lett.* **2011**, *514*, 274−277.
(13) Thun, J.; Seyfarth, L.; Butterhof, C.; Senker, J.; Dinnebier, R. E.; Breu, J. Wöhler and Liebig revisited: 176 years of polymorphism in benzamide - and the story still continues! *Cryst. Growth Des.* **2009**, *9*, 2435−2441.
(14) Ectors, P.; Ectors, D.; Zahn, D. Structure and interactions in benzamide molecular crystals. *Mol. Simul.* **2013**, *39*, 1079−1083.
(15) Johansson, K. E.; Van De Streek, J. Revision of the crystal structure of the first molecular polymorph in history. *Cryst. Growth Des.* **2016**, *16*, 1366−1370.
(16) Higgins, J. B.; LaPierre, R. B.; Schlenker, J. L.; Rohrman, A. C.; Wood, J. D.; Kerr, G. T.; Rohrbaugh, W. J. The framework topology of zeolite beta. *Zeolites* **1988**, *8*, 446−452.
(17) Lobo, R. F.; van Koningsveld, H. New description of the disorder in zeolite ZSM-48. *J. Am. Chem. Soc.* **2002**, *124*, 13222−13230.
(18) Baerlocher, C.; Weber, T.; McCusker, L. B.; Palatinus, L.; Zones, S. I. Unraveling the perplexing structure of the zeolite SSZ-57. *Science* **2011**, *333*, 1134−1137.
(19) Rozhdestvenskaya, I. V.; Mugnaioli, E.; Schowalter, M.; Schmidt, M. U.; Czank, M.; Depmeier, W.; Rosenauer, A. The structure of denisovite, a fibrous nanocrystalline polytypic disordered 'very complex' silicate, studied by a synergistic multi-disciplinary approach employing methods of electron crystallography and X-ray powder diffraction. *IUCrJ* **2017**, *4*, 223−242.
(20) Cichocka, M. O.; Lorgouilloux, Y.; Smeets, S.; Su, J.; Wan, W.; Caullet, P.; Bats, N.; McCusker, L. B.; Paillaud, J.-L.; Zou, X. Multidimensional disorder in zeolite IM-18 revealed by combining transmission electron microscopy and X-ray powder diffraction analyses. *Cryst. Growth Des.* **2018**, *18*, 2441−2451.
(21) Bürgi, H.-B.; Hostettler, M.; Birkedal, H.; Schwarzenbach, D. Stacking disorder: the hexagonal polymorph of tris(bicyclo[2.1.1]-hexeno)benzene and related examples. *Z. Kristallogr. Cryst. Mater.* **2005**, *220*, 1066−1075.
(22) Schmidt, M. U.; Glinnemann, J. Explanation for the stacking disorder in tris(bicyclo[2.1.1]hexeno)benzene using lattice-energy minimisations. *Z. Kristallogr. - Cryst. Mater.* **2012**, *227*, 805−818.
(23) Baias, M.; Dumez, J.-N.; Svensson, P. H.; Schantz, S.; Day, G. M.; Emsley, L. De Novo Determination of the Crystal Structure of a Large Drug Molecule by Crystal Structure Prediction-Based Powder NMR Crystallography. *J. Am. Chem. Soc.* **2013**, *135*, 17501−17507.
(24) Bhardwaj, R. M.; McMahon, J. A.; Nyman, J.; Price, L. S.; Konar, S.; Oswald, I. D. H.; Pulham, C. R.; Price, S. L.; Reutzel-Edens, S. M. A Prolific Solvate Former, Galunisertib, under the Pressure of Crystal Structure Prediction, Produces Ten Diverse Polymorphs. *J. Am. Chem. Soc.* **2019**, *141*, 13887−13897.
(25) Hofstetter, A.; Balodis, M.; Paruzzo, F. M.; Widdifield, C. M.; Stevanato, G.; Pinon, A. C.; Bygrave, P. J.; Day, G. M.; Emsley, L. Rapid Structure Determination of Molecular Solids Using Chemical Shifts Directed by Unambiguous Prior Constraints. *J. Am. Chem. Soc.* **2019**, *141*, 16624−16634.
(26) Braun, D. E.; Rivalta, A.; Giunchi, A.; Bedoya-Martinez, N.; Schrode, B.; Venuti, E.; Della Valle, R. G.; Werzer, O. Surface Induced Phenytoin Polymorph. 1. Full Structure Solution by Combining Grazing Incidence X-ray Diffraction and Crystal Structure Prediction. *Cryst. Growth Des.* **2019**, *19*, 6058−6066.
(27) Gryn'ova, G.; Lin, K.-H.; Corminboeuf, C. Read between the Molecules: Computational Insights into Organic Semiconductors. *J. Am. Chem. Soc.* **2018**, *140*, 16370−16386.
(28) Purdum, G. E.; Telesz, N. G.; Jarolimek, K.; Ryno, S. M.; Gessner, T.; Davy, N. C.; Petty, A. J.; Zhen, Y.; Shu, Y.; Facchetti, A.; Collis, G. E.; Hu, W.; Wu, C.; Anthony, J. E.; Weitz, R. T.; Risko, C.; Loo, Y.-L. Presence of Short Intermolecular Contacts Screens for Kinetic Stability in Packing Polymorphs. *J. Am. Chem. Soc.* **2018**, *140*, 7519−7525.
(29) Shtukenberg, A. G.; Punin, Y. O.; Gujral, A.; Kahr, B. Growth actuated bending and twisting of single crystals. *Angew. Chem., Int. Ed.* **2014**, *53*, 672−699.
(30) Jackson, C. L.; McKenna, G. B. The melting behavior of organic materials confined in porous solids. *J. Chem. Phys.* **1990**, *93*, 9002−9011.
(31) Jackson, C. L.; McKenna, G. B. Vitrification and crystallization of organic liquids confined to nanoscale pores. *Chem. Mater.* **1996**, *8*, 2128−2137.
(32) van Eijck, B. P.; Kroon, J. UPACK program package for crystal structure prediction: Force fields and crystal structure generation for small carbohydrate molecules. *J. Comput. Chem.* **1999**, *20*, 799−812.

https://dx.doi.org/10.1021/acs.cgd.0c00096
Cryst. Growth Des. 2020, 20, 2670−2682

(33) Wang, J.; Wolf, R. M.; Caldwell, J. W.; Kollman, P. A.; Case, D. A. Development and testing of a general amber force field. *J. Comput. Chem.* **2004**, *25*, 1157−1174.
(34) Bayly, C. I.; Cieplak, P.; Cornell, W.; Kollman, P. A. A well-behaved electrostatic potential based method using charge restraints for deriving atomic charges: the RESP model. *J. Phys. Chem.* **1993**, *97*, 10269−10280.
(35) Frisch, M. J.; Trucks, G. W.; Schlegel, H. B.; Scuseria, G. E.; Robb, M. A.; Cheeseman, J. R.; Scalmani, G.; Barone, V.; Mennucci, B.; Petersson, G. A.; Nakatsuji, H.; Caricato, M.; Li, X.; Hratchian, H. P.; Izmaylov, A. F.; Bloino, J.; Zheng, G.; Sonnenberg, J. L.; Hada, M.; Ehara, M.; Toyota, K.; Fukuda, R.; Hasegawa, J.; Ishida, M.; Nakajima, T.; Honda, Y.; Kitao, O.; Nakai, H.; Vreven, T.; Montgomery, J. A. J.; Peralta, J. E.; Ogliaro, F.; Bearpark, M.; Heyd, J. J.; Brothers, E.; Kudin, K. N.; Staroverov, V. N.; Kobayashi, R.; Normand, J.; Raghavachari, K.; Rendell, A.; Burant, J. C.; Iyengar, S. S.; Tomasi, J.; Cossi, M.; Rega, N.; Millam, J. M.; Klene, M.; Knox, J. E.; Cross, J. B.; Bakken, V.; Adamo, C.; Jaramillo, J.; Gomperts, R.; Stratmann, R. E.; Yazyev, O.; Austin, A. J.; Cammi, R.; Pomelli, C.; Ochterski, J. W.; Martin, R. L.; Morokuma, K.; Zakrzewski, V. G.; Voth, G. A.; Salvador, P.; Dannenberg, J. J.; Dapprich, S.; Daniels, A. D.; Farkas, Ö.; Foresman, J. B.; Ortiz, J. V.; Cioslowski, J.; Fox, D. J. *Gaussian 09*, rev. D.01; Gaussian, Inc.: Wallingford, CT, 2009.
(36) Hutter, J.; Iannuzzi, M.; Schiffmann, F.; VandeVondele, J. CP2K: Atomistic simulations of condensed matter systems. *WIREs Comput. Mol. Sci.* **2014**, *4*, 15−25.
(37) Lippert, G.; Hutter, J.; Parrinello, M. A hybrid Gaussian and plane wave density functional scheme. *Mol. Phys.* **1997**, *92*, 477−488.
(38) VandeVondele, J.; Krack, M.; Mohamed, F.; Parrinello, M.; Chassaing, T.; Hutter, J. QUICKSTEP: Fast and accurate density functional calculations using a mixed Gaussian and plane waves approach. *Comput. Phys. Commun.* **2005**, *167*, 103−128.
(39) Perdew, J. P.; Burke, K.; Ernzerhof, M. Generalized gradient approximation made simple. *Phys. Rev. Lett.* **1996**, *77*, 3865−3868.
(40) VandeVondele, J.; Hutter, J. Gaussian basis sets for accurate calculations on molecular systems in gas and condensed phases. *J. Chem. Phys.* **2007**, *127*, 114105.
(41) Goedecker, S.; Teter, M.; Hutter, J. Separable dual-space Gaussian pseudopotentials. *Phys. Rev. B: Condens. Matter Mater. Phys.* **1996**, *54*, 1703−1710.
(42) Krack, M. Pseudopotentials for H to Kr optimized for gradient-corrected exchange-functionals. *Theor. Chem. Acc.* **2005**, *114*, 145−152.
(43) Grimme, S.; Antony, J.; Ehrlich, S.; Krieg, H. A consistent and accurate *ab initio* parametrization of density functional dispersion correction (DFT-D) for the 94 elements H-Pu. *J. Chem. Phys.* **2010**, *132*, 154104.
(44) Grimme, S.; Ehrlich, S.; Goerigk, L. Effect of the damping function in dispersion corrected density functional theory. *J. Comput. Chem.* **2011**, *32*, 1456−1465.
(45) Sheldrick, G. M. Crystal structure refinement with SHELXL. *Acta Crystallogr., Sect. C: Struct. Chem.* **2015**, *C71*, 3−8.
(46) Proffen, T.; Neder, R. B. DISCUS: A program for diffuse scattering and defect-structure simulation. *J. Appl. Crystallogr.* **1997**, *30*, 171−175.
(47) Butler, B. D.; Welberry, T. R. Calculation of diffuse scattering from simulated disordered crystals: a comparison with optical transforms. *J. Appl. Crystallogr.* **1992**, *25*, 391−399.
(48) Weber, T.; Schaub, P.; Steurer, W. 3D-PDF analysis of single-crystal diffuse scattering on the example of disordered quasicrystals. *Acta Crystallogr., Sect. A: Found. Crystallogr.* **2008**, *64*, C131−C132.
(49) Shtukenberg, A. G.; Tan, M.; Vogt-Maranto, L.; Chan, E. J.; Xu, W.; Yang, J.; Tuckerman, M. E.; Hu, C. T.; Kahr, B. Melt crystallization for paracetamol polymorphism. *Cryst. Growth Des.* **2019**, *19*, 4070−4080.
(50) Shtukenberg, A. G.; Gunn, E.; Yu, L.; Kahr, B. Glass-crystal growth mode for testosterone propionate. *Cryst. Growth Des.* **2011**, *11*, 4458−4462.
(51) Shtukenberg, A. G.; Hu, C. T.; Zhu, Q.; Schmidt, M. U.; Xu, W.; Tan, M.; Kahr, B. The third ambient aspirin polymorph. *Cryst. Growth Des.* **2017**, *17*, 3562−3566.
(52) Shtukenberg, A. G.; Zhu, Q.; Carter, D. J.; Vogt, L.; Hoja, J.; Schneider, E.; Song, H.; Pokroy, B.; Polishchuk, I.; Tkatchenko, A.; Oganov, A. R.; Rohl, A. L.; Tuckerman, M. E.; Kahr, B. Powder diffraction and crystal structure prediction identify four new coumarin polymorphs. *Chem. Sci.* **2017**, *8*, 4926−4940.
(53) Zhu, Q.; Shtukenberg, A. G.; Carter, D. J.; Yu, T.-Q.; Yang, J.; Chen, M.; Raiteri, P.; Oganov, A. R.; Pokroy, B.; Polishchuk, I.; Bygrave, P. J.; Day, G. M.; Rohl, A. L.; Tuckerman, M. E.; Kahr, B. Resorcinol crystallization from the melt: A new ambient phase and new "riddles. *J. Am. Chem. Soc.* **2016**, *138*, 4881−4889.
(54) Yang, J.; Hu, C. T.; Zhu, X.; Zhu, Q.; Ward, M. D.; Kahr, B. DDT Polymorphism and the lethality of crystal forms. *Angew. Chem.* **2017**, *129*, 10299−10303.
(55) Ha, J.-M.; Wolf, J. H.; Hillmyer, M. A.; Ward, M. D. Polymorph selectivity under nanoscopic confinement. *J. Am. Chem. Soc.* **2004**, *126*, 3382−3383.
(56) Beiner, M.; Rengarajan; Pankaj, S.; Enke, D.; Steinhart, M. Manipulating the crystalline state of pharmaceuticals by nanoconfinement. *Nano Lett.* **2007**, *7*, 1381−1385.
(57) Ha, J.-M.; Hamilton, B. D.; Hillmyer, M. A.; Ward, M. D. Phase behavior and polymorphism of organic crystals confined within nanoscale chambers. *Cryst. Growth Des.* **2009**, *9*, 4766−4777.
(58) Jiang, Q.; Ward, M. D. Crystallization under nanoscale confinement. *Chem. Soc. Rev.* **2014**, *43*, 2066−2079.
(59) Nartowski, K. P.; Tedder, J.; Braun, D. E.; Fábián, L.; Khimyak, Y. Z. Building solids inside nano-space: from confined amorphous through confined solvate to confined 'metastable' polymorph. *Phys. Chem. Chem. Phys.* **2015**, *17*, 24761−24773.
(60) Nartowski, K. P.; Malhotra, D.; Hawarden, L. E.; Fábián, L.; Khimyak, Y. Z. Nanocrystallization of rare tolbutamide form V in mesoporous MCM-41 silica. *Mol. Pharmaceutics* **2018**, *15*, 4926−4932.
(61) Belenguer, A. M.; Lampronti, G. I.; Cruz-Cabeza, A. J.; Hunter, C. A.; Sanders, J. K. M. Solvation and surface effects on polymorph stabilities at the nanoscale. *Chem. Sci.* **2016**, *7*, 6617−6627.
(62) Ha, J.-M.; Hillmyer, M. A.; Ward, M. D. Thermotropic properties of organic nanocrystals embedded in ultrasmall crystallization chambers. *J. Phys. Chem. B* **2005**, *109*, 1392−1399.
(63) Jackson, C. L.; McKenna, G. B. The glass transition of organic liquids confined to small pores. *J. Non-Cryst. Solids* **1991**, *131*, 221−224.
(64) Gibbs, J. W. *The collected works of J. Willard Gibbs: Thermodynamics*; Yale University Press, 1928; Vol. *1*.
(65) Thomson, J. J. *Applications of dynamics to physics and chemistry*; Macmillan, 1888.
(66) Defay, R.; Bellemans, A.; Prigogine, I. *Surface tension and adsorption*; Longmans, 1966.
(67) Digilov, R. M. Semi-empirical model for prediction of crystal−melt interfacial tension. *Surf. Sci.* **2004**, *555*, 68−74.
(68) Sonnenberger, N.; Anders, N.; Golitsyn, Y.; Steinhart, M.; Enke, D.; Saalwächter, K.; Beiner, M. Pharmaceutical nanocrystals confined in porous host systems − interfacial effects and amorphous interphases. *Chem. Commun.* **2016**, *52*, 4466−4469.
(69) Le Bail, A. Monte Carlo indexing with McMaille. *Powder Diffr.* **2004**, *19*, 249−254.
(70) *TOPAS V4.2: General profile and structure analysis software for powder diffraction data*. Bruker AXS, Karlsruhe, Germany, 2008.
(71) van Eijck, B. P.; Kroon, J. UPACK program package for crystal structure prediction: Force fields and crystal structure generation for small carbohydrate molecules. *J. Comput. Chem.* **1999**, *20*, 799−812.
(72) Wang, J.; Wolf, R. M.; Caldwell, J. W.; Kollman, P. A.; Case, D. A. Development and testing of a general amber force field. *J. Comput. Chem.* **2004**, *25*, 1157−1174.
(73) Etter, M. C.; MacDonald, J. C.; Bernstein, J. Graph-set analysis of hydrogen-bond patterns in organic crystals. *Acta Crystallogr., Sect. B: Struct. Sci.* **1990**, *46*, 256−262.

https://dx.doi.org/10.1021/acs.cgd.0c00096
Cryst. Growth Des. 2020, 20, 2670−2682

(74) Sinnokrot, M. O.; Sherrill, C. D. High-accuracy quantum mechanical studies of π-π interactions in benzene dimers. *J. Phys. Chem. A* **2006**, *110*, 10656−10668.
(75) DiStasio, R. A.; von Helden, G.; Steele, R. P.; Head-Gordon, M. On the T-shaped structures of the benzene dimer. *Chem. Phys. Lett.* **2007**, *437*, 277−283.
(76) Goossens, D. J.; Heerdegen, A. P.; Chan, E. J.; Welberry, T. R. Monte Carlo modeling of diffuse scattering from single crystals: The Program ZMC. *Metall. Mater. Trans. A* **2011**, *42*, 23−31.
(77) Chan, E. J.; Welberry, T. R.; Heerdegen, A. P.; Goossens, D. J. Diffuse scattering study of aspirin forms (I) and (II). *Acta Crystallogr., Sect. B: Struct. Sci.* **2010**, *66*, 696−707.
(78) Chan, E. J.; Welberry, T. R.; Goossens, D. J.; Heerdegen, A. P.; Beasley, A. G.; Chupas, P. J. Single-crystal diffuse scattering studies on polymorphs of molecular crystals. I. The room-temperature polymorphs of the drug benzocaine. *Acta Crystallogr., Sect. B: Struct. Sci.* **2009**, *65*, 382−392.
(79) Plimpton, S. Fast parallel algorithms for short-range molecular dynamics. *J. Comput. Phys.* **1995**, *117*, 1−19.
(80) Yu, T.-Q.; Tuckerman, M. E. Temperature-accelerated method for exploring polymorphism in molecular crystals based on free energy. *Phys. Rev. Lett.* **2011**, *107*, 015701.
(81) Schneider, E.; Vogt, L.; Tuckerman, M. E. Exploring polymorphism of benzene and naphthalene with free energy based enhanced molecular dynamics. *Acta Crystallogr., Sect. B: Struct. Sci., Cryst. Eng. Mater.* **2016**, *72*, 542−550.

https://dx.doi.org/10.1021/acs.cgd.0c00096
Cryst. Growth Des. 2020, 20, 2670−2682